The similarity between the A_6C_{60} spectra doped with different alkali metals again indicates that the observed modes are due only to the C_{60} molecule, and that there are no observable A-C_{60} modes above 100 cm^{-1}. The mode at 270 cm^{-1} has a resolution-limited FWHM for Cs_6C_{60}, is broadened in Rb_6C_{60}, and is a doublet in K_6C_{60}. The high-frequency mode of the doublet may result from a two-phonon process involving a low energy–A-C_{60} mode, the frequency of which will increase as the ion mass is reduced. Finally, we also point out that the four modes observed above 1600 cm^{-1} in Cs_6C_{60} (and weakly in Rb_6C_{60} and K_6C_{60}) appear to be sum modes of the two lowest frequency H_g modes (271 cm^{-1} and 428 cm^{-1}) and the two highest frequency H_g modes (1383 cm^{-1} and 1478 cm^{-1}). If this is the case, it is not clear that these modes should be broadened in the same way as the zone center (one-phonon) modes by the electron phonon coupling (*9–10*).

The Raman spectra of Na_xC_{60} are consistent with the above results with the following exceptions. Although banding was observed in these films upon doping, intermediate values of the A_g mode frequency were observed between 1448 cm^{-1} and 1455 cm^{-1}. Also, a time dependence of this mode frequency has been observed in the laser beam at the power densities used in the studies of the K-, Rb-, and Cs-doped films. These results indicate that Na-doped C_{60} either does not phase separate in Na_xC_{60} with $0 \leq x \leq 3$ or that phases other than $x = 0$ and $x = 3$ are stable. For Na_6C_{60} the A_g mode is at 1434 cm^{-1}, significantly higher than the 1430 ± 1 cm^{-1} observed in the other A_6C_{60} materials. This is consistent with incomplete electron transfer in Na_xC_{60}, which may be responsible for the lack of superconductivity above 4 K (*11*). Further work is needed to clarify the phase diagram and electronic structure of the Na_xC_{60} compounds.

REFERENCES AND NOTES

1. R. C. Haddon *et al.*, *Nature* **350**, 320 (1991).
2. A. F. Hebard *et al.*, *ibid.*, p. 600.
3. H. W. Kroto, J. R. Heath, S. C. O'Brien, R. F. Curl, R. E. Smalley, *ibid.* **318**, 162 (1991).
4. W. Krätschmer, L. D. Lamb, K. Fostiropoulos, D. R. Huffman, *ibid.* **347**, 354 (1990).
5. M. J. Rosseinsky *et al.*, *Phys. Rev. Lett.* **66**, 2830 (1991).
6. K. Holczer *et al.*, *Science* **252**, 1154 (1991).
7. S. P. Kelty, C.-C. Chen, C. M. Lieber, *Nature* **352**, 223 (1991).
8. K. Tanigaki *et al.*, *ibid.*, p. 222.
9. C. M. Varma, J. Zaanen, K. Raghavachari, *Science* **254**, 989 (1991).
10. M. A. Schluter, M. Lannoo, M. K. Needels, G. A. Baraff, in preparation.
11. S. H. Glarum, S. J. Duclos, R. C. Haddon, in preparation.
12. G. P. Kochanski, A. F. Hebard, R. C. Haddon, A. T. Fiory, in preparation.
13. R. Tycko *et al.*, *Science* **253**, 884 (1991).
14. R. M. Fleming *et al.*, *Nature* **352**, 701 (1991).
15. S. J. Duclos, R. C. Haddon, S. H. Glarum, A. F. Hebard, K. B. Lyons, *Solid State Commun.*, in press.
16. D. S. Bethune *et al.*, *Chem. Phys. Lett.* **179**, 181 (1991).
17. S. H. Tolbert, A. P. Alivistatos, H. Lorenano, M. Kruger, R. Jeanloz, in preparation.
18. P. B. Allen, *Phys. Rev. B* **6**, 2577 (1972).
19. O. Zhou *et al.*, *Nature* **351**, 462 (1991).

20. We thank R. M. Fleming, M. Schluter, P. Sulewski, R. Tycko, and C. Varma for valuable discussions.

2 October 1991; accepted 29 October 1991

Molecular Architecture and Electrostatic Properties of a Bacterial Porin

M. S. WEISS, U. ABELE, J. WECKESSER, W. WELTE, E. SCHILTZ, G. E. SCHULZ*

The integral membrane protein porin from *Rhodobacter capsulatus* consists of three tightly associated 16-stranded β barrels that give rise to three distinct diffusion channels for small solutes through the outer membrane. The x-ray structure of this porin has revealed details of its shape, the residue distributions within the pore and at the membrane-facing surface, and the location of calcium sites. The electrostatic potential has been calculated and related to function. Moreover, potential calculations were found to predict the Ca^{2+} sites.

GRAM-NEGATIVE BACTERIA PROTECT themselves from hostile environments by an outer membrane. This membrane, however, has to be permeable to polar, low molecular mass solutes including nutrients. For this purpose it contains channel-forming proteins called porins, which are usually trimeric with relative subunit masses between 30,000 and 50,000 and solute exclusion limits around 600 daltons (*1, 2*). Spectroscopic (*3*) and electron microscopic studies (*4, 5*) have yielded a rather general description of their architecture. Several porins have been crystallized and subjected to x-ray diffraction analyses (*6–10*). Among these, the crystals of porin from the photosynthetic bacterium *Rhodobacter capsulatus* strain 37b4 could be analyzed to atomic resolution (*8, 11–14*). We describe this porin with respect to its shape, its pore properties, its outer surface, and its electrostatic properties.

The present crystallographic *R* factor of the porin model (*15*) is 0.191 in the resolution range from 10 to 1.8 Å. As displayed in Fig. 1, a porin subunit consists of 16 β strands with lengths ranging from 6 to 17 residues. The 16 strands form a completely antiparallel β barrel, in which all strands are connected to their neighbors. Three of the 15 connecting loops contain short α helices. The seven loops at the bottom of the barrel (Fig. 1) are short (two to five residues) whereas the eight loops at the top end are generally longer (5 to 44 residues, with an average of 14 residues). The tilting angles of the β strands against the trimer axis, which coincides with the membrane normal, vary from 30° to 60°. The model contains three calcium ions: two are located within the pore (Ca-I and Ca-II) and the third one (Ca-III) at the subunit interface. The presumed detergent molecule of the model binds in a hydrophobic pocket below helix α3.

The shape of a porin subunit is represented with a low-resolution electron density map displayed at the 1σ level. A cut through the center of one subunit yields two halves depicted side by side in Fig. 2. Four cutting areas are created: no. 1, the β barrel with a short height at the subunit interfaces near the molecular threefold axis; no. 2, the β barrel at its maximum height at the membrane-facing side; no. 3, the 44-residue loop between strands β5 and β6 inside the β barrel; and no. 4, the second largest loop (20 residues between strands β11 and β12) forming a small globule at the top end of the β barrel.

The association of porin subunits to the trimer can be done by a superposition of both indicated axes, followed by a rotation of the left-hand side by 60° around this axis. This connects the rear β barrel walls at the heights of the indicated discontinuous lines (see Fig. 5 for verification). Thus, a common channel of the three subunits is formed that extends from the upper discontinuous line to the upper end of section area no. 1. This common channel leads into three distinct eyelets (one per subunit) that define

M. S. Weiss, U. Abele, E. Schiltz, G. E. Schulz, Institut für Organische Chemie und Biochemie, Albertstrasse 21, D-7800 Freiburg im Breisgau, Federal Republic of Germany.
J. Weckesser, Institut für Biologie II, Mikrobiologie Schänzlestrasse 1, D-7800 Freiburg im Breisgau, Federal Republic of Germany.
W. Welte, Institut für Biophysik und Strahlenbiologie, Albertstrasse 23, D-7800 Freiburg im Breisgau, Federal Republic of Germany.

*To whom correspondence should be addressed.

the solute exclusion size. Further down, the eyelets open up continuously over a vertical distance of ~10 Å to form cone-like structures, which again are followed by straight cylinders with axial lengths of ~10 Å at the bottom end of the channel. These zones have formerly been named "triple," "eyelet," "cone," and "pipe" (*11*).

As depicted in Fig. 3 the eyelet is lined almost exclusively by ionogenic groups that segregate into positively and negatively charged surface segments. The positive part is closer to the trimer center and consists of two Lys and three Arg residues on β strands and one His on a loop. The negatively charged surface segment contains seven Asp and four Glu residues on the 13-residue loop between strands β3 and β4 as well as on the 44-residue loop between strands β5 and β6. This large local surplus of negative charges is partially compensated by the calcium ions Ca-I and Ca-II. As described below, there is a third Ca^{2+}-site at the eyelet, Ca-IV, which is only occupied at higher calcium concentrations (see Fig. 5).

Accounting for Ca-I and Ca-II of the model, we find that the eyelet is lined by seven negative charges on one side and six positive charges on the other. This arrangement causes a transversal electric field across the pore, which is obviously strong, as it allows the guanidino groups to remain side by side at van der Waals distance although they are certainly charged (Fig. 3). Due to the observed rigidity of these side chains the opening of the pore is reduced to about 7 Å by 9 Å. Even small polar solutes therefore have to lose transiently at least parts of their hydration shell when penetrating. Conceivably, the transversal field plays a part in this dehydration. An appreciable influence of charged residues on solute selection had also been suggested by experiments on other porins (*16*, *17*).

The arrangement of charges at the eyelet (Fig. 3) suggests that electric fields are of functional importance. Therefore, we calculated the electrostatic potential of trimeric porin (*18–23*). This calculation yielded a rather weak negative potential at the bottom of the trimer (Fig. 4). Moving upward the potential becomes weakly positive followed by a neutral layer and then by the minimum of the potential of about $-8\ kT$ (k, Boltzmann's constant, and T, absolute temperature) at the height of the eyelet. At the top end of the trimer there is a large area of

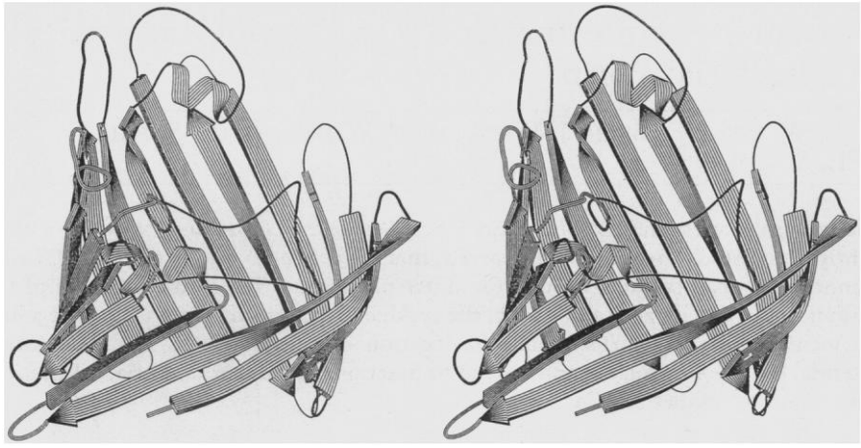

Fig. 1. Stereo view of the chain fold of one subunit of the porin of *Rhodobacter capsulatus* as drawn with the program RIBBON (*31*). Indicated are β strands (arrows) and α helices. The view is approximately from the threefold axis. The amino and carboxyl termini are adjacent and at the front side. The large loop between strands β5 and β6 lining the inside of the 16-stranded β barrel forms the solute size defining eyelet of the pore. Clearly visible is the smooth-rimmed bottom end of the barrel, which faces the periplasm, and the rugged top end, which faces the external medium (*29*, *30*).

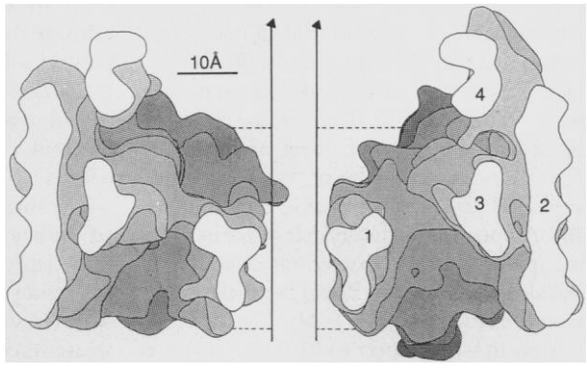

Fig. 2. General shape of the pore as illustrated by a series of slices representing all density above the 1σ-level of a low-resolution (6 Å) F_{calc} $\exp i\alpha_{calc}$ electron density map of an isolated subunit; F_{calc} and α_{calc} are calculated from the refined positions of the polypeptide atoms (*14*). The center of mass of the subunit is at (−0.1, −0.3, 0.0); the slices are 3.6 Å thick and lie parallel to the y,z-plane of the unit cell. The cut dividing one subunit into two halves runs through the pore center. The two halves are depicted like a cut apple put on a table. For reference, the threefold axis at (0.0, 0.0) is indicated, and the sectional areas (unshaded) are given on both halves and numbered (see text). Depth is represented by shading. The eyelet is located between areas no. 1 and no. 3. This representation is preferable to conventional surface drawings as it accounts for the atom mobilities; more mobile atoms contribute less.

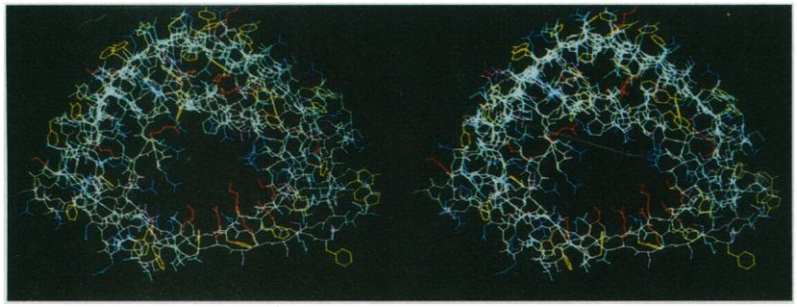

Fig. 3. Stereo view along the threefold axis from the external medium onto a single subunit as displayed by the program BRAGI (*32*). The side chains are color coded: negatively charged, positively charged, aromatic, polar, and nonpolar side chains are blue, red, yellow, purple, and light blue, respectively. Clearly visible is the juxtaposition of a ring of negatively charged residues at the upper side and a group of positively charged residues at the lower side, both lining the eyelet, that is, the solute-exclusion size defining part of the pore.

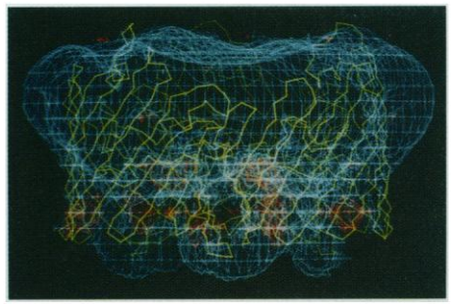

Fig. 4. Electrostatic potential of a porin trimer (given as Cα backbone) calculated as described (*18*). Potential surfaces are drawn at energies of $-1\ kT$ (blue) and $+1\ kT$ (red). The threefold axis lies vertical in the plane of the page.

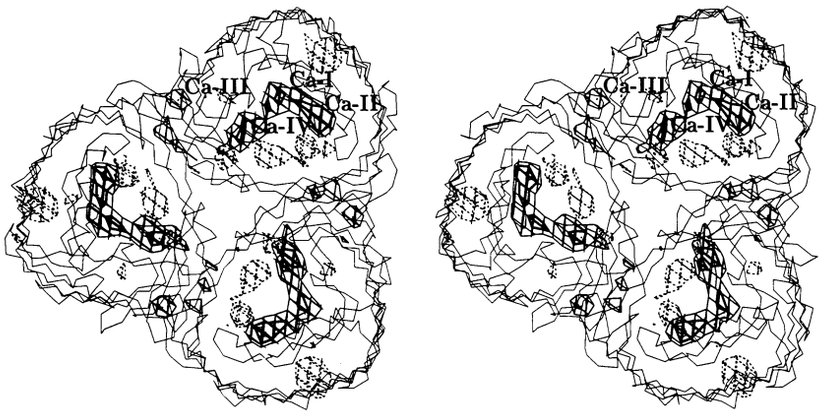

Fig. 5. Prediction of Ca^{2+} sites from the electrostatic potential. The potential was calculated as described (*18*) but without any Ca^{2+} ion. The potential surfaces are drawn at the observed extreme levels of $-7\ kT$ (thick lines) and $-6\ kT$ (medium lines), as well as at $+1\ kT$ (discontinuous lines) within trimeric porin represented by its Cα backbone. The four Ca^{2+} positions [Ca-I, Ca-II, and Ca-III from the model (*15*); Ca-IV as predicted and observed (*24*)] are indicated by labels. The fit between the potential minima and the observed Ca^{2+} sites is better than 1 Å.

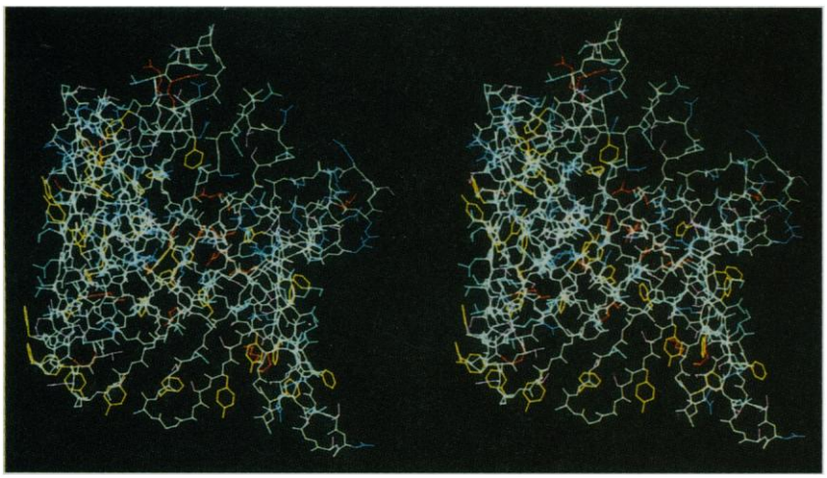

Fig. 6. Stereo view of the full-atom model of a porin subunit with the same color code as in Fig. 3 (*32*). The threefold axis is nearly vertical. The two rings of aromatic residues, the nonpolar surface zone, and the ring of mostly negatively charged residues can be recognized.

negative potential at the $-1\ kT$ level. Since this end faces the external space, the potential probably attracts cations from the environment, contributing to the slight cation selectivity of this porin. The pocket with the lowest potential was located between carboxyl groups at the eyelet. We therefore suspected that it indicates a fourth, nonoccupied Ca^{2+} binding site, Ca-IV. At higher calcium concentrations this position was indeed found occupied (*24*).

The successful prediction of Ca-IV made us wonder whether we could also derive the other Ca^{2+} sites from the electrostatic field. We therefore recalculated this field as described (*18*) but without the three Ca^{2+} ions of the model. As shown in Fig. 5, we found $-7\ kT$ potential wells at Ca-I, Ca-II, and again at Ca-IV, all at the eyelet, and a $-6\ kT$ well at Ca-III within the interface. Accordingly, the Ca^{2+} binding sites can be efficiently predicted from electrostatic calculations, adding a new aspect to previous attempts for predicting metal ion positions in proteins (*25*).

The outer surface of the β barrel faces the barrels of the other subunits and the membrane (Fig. 5). The intersubunit contact areas cover about one-third of this surface and are mostly polar, involving salt bridges between the amino- and carboxyl-termini of different subunits, a number of hydrogen bonds, and the interfacial Ca-III. This Ca^{2+} ion was presumably extracted by EDTA in the early preparation procedure, giving rise to monomeric porin chains found in SDS-gel electrophoresis (*8*, *11*, *12*). The nature and the arrangement of the membrane-facing side chains are illustrated in Fig. 6. The exposed part of the surface can be vertically subdivided into four different zones. Starting from the bottom, the first zone is characterized by the presence of many aromatic residues, such as Phe^{67}, Tyr^{121}, Tyr^{123}, Phe^{128}, Tyr^{156}, Phe^{158}, Tyr^{161}, Phe^{192}, Phe^{240}, and Tyr^{269}. The Tyr side chains all point downward (away from the nonpolar part of the membrane), and the Phe residues point upward. These residues form a ring around the porin trimer. A second ring of aromatics is found in the third zone (counted from the bottom), which includes the residues Tyr^{167}, Tyr^{201}, Tyr^{232}, Tyr^{263}, Tyr^{14}, and Trp^{19} but, remarkably, no Phe residues.

Between these two rings of aromatics one finds the expected nonpolar zone made up mainly of Leu, Val, and Ala but only few Ile residues. This zone has an axial length of ~12 Å so that the total height of the nonpolar surface sums up to ~25 Å. This value is in agreement with the thickness of the nonpolar layer as derived, for instance, from small-angle x-ray diffraction analyses of artificial membranes (*26*). As judged from the distribution of polar and nonpolar atoms over the outer surface of porin, all of these aromatic residues occur right at the borderline between the polar and nonpolar parts of the membrane. This peculiar observation remains unexplained. The aromatic-nonpolar-aromatic ring pattern had also been observed for the bacterial photoreaction center (*27*) and for bacteriorhodopsin (*28*), although in a less clear manner.

The three rings are followed by a fourth ring of residues at the upper part of the outer surface of the barrel that is characterized by about 16 negative and 3 positive charges (Fig. 6). The large excess of negative charges in this ring adds to the broad negative potential trough at $-1\ kT$ in this region (Fig. 4). The numerous carboxyls are likely to interact with polar parts of the lipopolysaccharides of the outer bacterial membrane. This interaction could well involve further Ca^{2+} ions.

Since the outer surface of porin must match the membrane properties, the zone of nonpolar residues reveals the axial position of porin in the membrane. The rough (here top) ends of the barrels contain the large strongly polar loops that face the external medium (*29*, *30*); the smooth (bottom) ends of the barrels, which are much less polar, face the periplasm. Since the bottom end is close to the nonpolar surface zone, porin sits in the membrane like a funnel with protrusions to the external but not to the periplasmic side. The reported porin structure now provides a firm base for functional studies on this and on related membrane channels.

REFERENCES AND NOTES

1. H. Nikaido and M. Vaara, *Microbiol. Rev.* **49**, 1 (1985).
2. R. Benz and K. Bauer, *Eur. J. Biochem.* **176**, 1 (1988).

3. E. Nabedryk, R. M. Garavito, J. Breton, *Biophys. J.* **53**, 671 (1988).
4. A. Engel, A. Massalski, H. Schindler, D. L. Dorset, J. P. Rosenbusch, *Nature* **317**, 643 (1985).
5. B. K. Jap, P. J. Walian, K. Gehring, *ibid.* **350**, 167 (1991).
6. R. M. Garavito and J. P. Rosenbusch, *J. Cell. Biol.* **86**, 327 (1980).
7. R. M. Garavito, J. Jenkins, J. N. Jansonius, R. Karlsson, J. P. Rosenbusch, *J. Mol. Biol.* **164**, 313 (1983).
8. U. Nestel, T. Wacker, D. Woitzik, J. Weckesser, W. Kreutz, W. Welte, *FEBS Lett.* **242**, 405 (1989).
9. K. A. Stauffer, M. G. P. Page, A. Hardmeyer, T. A. Keller, R. A. Pauptit, *J. Mol. Biol.* **211**, 297 (1990).
10. R. A. Pauptit, H. Zhang, G. Rummel, T. Schirmer, J. N. Jansonius, J. Rosenbusch, *ibid.* **218**, 505 (1991).
11. M. S. Weiss, T. Wacker, J. Weckesser, W. Welte, G. E. Schulz, *FEBS Lett.* **267**, 268 (1990).
12. A. Kreusch, M. S. Weiss, W. Welte, J. Weckesser, G. E. Schulz, *J. Mol. Biol.* **217**, 9 (1991).
13. E. Schiltz, A. Kreusch, U. Nestel, G. E. Schulz, *Eur. J. Biochem.* **199**, 587 (1991).
14. M. S. Weiss *et al.*, *FEBS Lett.* **280**, 379 (1991).
15. Porin from *Rhodobacter capsulatus* strain 37b4 crystallizes in space group *R*3 with unit cell dimensions a_{hex} = 92.3 Å and c_{hex} = 146.2 Å and a solvent volume fraction of 69% at pH 7.2 and an ionic strength of 0.32 (20 mM tris-HCl and 300 mM LiCl) (*12*). The crystals diffract beyond 1.8 Å resolution. The molecular weight of one subunit is 31,536 as derived from the sequence of 301 residues (*13*). The structure had been solved and refined at 1.8 Å resolution with a 99% complete native data set composed of diffractometer data to 3.6 Å resolution and synchrotron data to 1.8 Å resolution with an overall R_{sym} of 0.067 in intensities (*14*). The present model contains 2219 protein atoms, 314 water molecules, three calcium ions, and a presumed detergent molecule that was modeled as a C_{16} aliphatic chain. The root-mean-square deviations of bond lengths and bond angles are 0.019 Å and 3.0°, respectively.
16. S. A. Benson, J. L. L. Occi, B. A. Sampson, *J. Mol. Biol.* **203**, 961 (1988).
17. K. Bauer, M. Struyve, D. Bosch, R. Benz, J. Tommassen, *J. Biol. Chem.* **264**, 16393 (1989).
18. The electrostatic field was calculated for trimeric porin with the native polypeptide structure including three Ca^{2+} ions, 53 water molecules with a crystallographic temperature factor below 30 Å^2, and the presumed detergent molecule. For this purpose we solved the linearized Poisson-Boltzmann equation using a finite difference algorithm on a grid of 65 by 65 by 65 sampling positions (*19*, *20*). The program was gratefully received from Karshikov and Ladenstein (*21*). The atomic radii and the partial atom charges were taken from the molecular dynamics program XPLOR (*22*). The discrete partial atom charges were fractionized and distributed over the eight nearest grid points. Side chains were taken as fully charged, and a surface probe radius of 1.6 Å and a Debye length of 8 Å (150 mM ionic strength) were used. Dielectric constants of 2 and 80 were assigned to the protein inside and outside, respectively. Dipoles of α helices and β-sheet strands were modeled as ±1/2 and ±1/15 unit charges at the amino and carboxyl termini, respectively (*23*). The initial boundary potential was calculated with a Debye-Hueckel equation (*19*) with a distance-dependent dielectric constant (ε = distance in angstroms) on a 65 by 65 by 65 grid with a mesh size of 5 Å. The mesh size was then reduced to 3.5 Å and finally to 2 Å, which still allowed for the recommended (*20*) minimum of two Debye lengths bulk solvent around the trimer.
19. J. Warwicker and H. C. Watson, *J. Mol. Biol.* **157**, 671 (1982).
20. I. Klapper, R. Hagstrom, R. Fine, K. Sharp, B. Honig, *Proteins* **1**, 47 (1986).
21. A. Karshikov and R. Ladenstein, *ibid.* **5**, 248 (1989).
22. A. T. Brünger, J. Kuriyan, M. Karplus, *Science* **235**, 458 (1987).
23. W. G. J. Hol, L. M. Halie, C. Sander, *Nature* **294**, 532 (1981).
24. In an additional experiment, porin was crystallized in the presence of 20 mM $CaCl_2$ and a data set was collected at 2.2 Å resolution on a Xentronics/Siemens area detector. The difference density showed a clear peak at the electrostatic well of Fig. 5 at the eyelet labeled Ca-IV, confirming the binding of a fourth Ca^{2+} ion. The calcium ions I, II, and III were found in the structure, although no calcium was added to the preparation and crystallization buffer.
25. M. M. Yamashita, L. Wesson, G. Eisenman, D. Eisenberg, *Proc. Natl. Acad. Sci. U.S.A.* **87**, 5648 (1990).
26. B. A. Lewis and D. M. Engelman, *J. Mol. Biol.* **166**, 211 (1983).
27. J. Deisenhofer, O. Epp, K. Miki, R. Huber, H. Michel, *Nature* **318**, 618 (1985).
28. R. Henderson, J. M. Baldwin, T. A. Ceska, F. Zemlin, E. Beckmann, K. H. Downing, *J. Mol. Biol.* **213**, 899 (1990).
29. J. Tommassen, in *Membrane Biogenesis*, vol. H16 of the *NATO ASI Series*, J. A. F. Op den Kamp, Ed. (Springer-Verlag, Berlin, 1988), p. 351.
30. W. Welte, M. S. Weiss, U. Nestel, J. Weckesser, E. Schiltz, G. E. Schulz, *Biochim. Biophys. Acta*, in press.
31. J. Priestle, *J. Appl. Crystallogr.* **21**, 572 (1988).
32. D. Schomburg and J. Reichelt, *J. Mol. Graphics* **6**, 161 (1988).
33. Coordinates are deposited in the Brookhaven Protein Data Bank (1 POR).

17 July 1991; accepted 16 October 1991

Heterogeneous Amino Acids in Ras and Rap1A Specifying Sensitivity to GAP Proteins

KE ZHANG, ALEX G. PAPAGEORGE, PATRICK MARTIN,*
WILLIAM C. VASS, ZOLTAN OLAH, PAUL G. POLAKIS,
FRANK MCCORMICK, DOUGLAS R. LOWY

Guanosine triphosphatase (GTPase) activity of Ras is increased by interaction with Ras-GAP (GTPase-activating protein) or with the GAP-related domain of the type 1 neurofibromatosis protein (NF1-GRD), but Ras is not affected by interaction with cytoplasmic and membrane forms of Rap-GAP; Rap1A, whose effector function can suppress transformation by Ras, is sensitive to both forms of Rap-GAP and resistant to Ras-GAP and NF1-GRD. A series of chimeric proteins composed of portions of Ras and Rap were constructed; some were sensitive to Ras-GAP but resistant to NF1-GRD, and others were sensitive to cytoplasmic Rap-GAP but resistant to membrane Rap-GAP. Sensitivity of chimeras to Ras-GAP and cytoplasmic Rap-GAP was mediated by amino acids that are carboxyl-terminal to the effector region. Residues 61 to 65 of Ras conferred Ras-GAP sensitivity, but a larger number of Rap1A residues were required for sensitivity to cytoplasmic Rap-GAP. Chimeras carrying the Ras effector region that were sensitive only to Ras-GAP or only to cytoplasmic Rap-GAP transformed NIH 3T3 cells poorly. Thus, distinct amino acids of Ras and Rap1A mediate sensitivity to each of the proteins with GAP activity, and transforming potential of Ras and sensitivity of Ras to Ras-GAP are at least partially independent properties.

THE RAS-RELATED GENES ENCODE A superfamily of proteins that are approximately 21 kD (p21), bind guanine nucleotides, and have intrinsic GTPase activity (*1*). The Ras protein can induce cellular transformation and is active when GTP is bound and inactive when GDP is bound. The intrinsic GTPase activities of Ras, Rap (also called p21 Krev-1 and smg-p21A), (*2–4*), and Rho can be accelerated by the distinct cellular proteins Ras-GAP, Rap-GAP, and Rho-GAP, respectively (*5–7*). The physiological function of the p21 and GAP proteins remains incompletely defined, but overexpression of Rap can suppress transformation by Ras.

K. Zhang, A. G. Papageorge, P. Martin, W. C. Vass, Z. Olah, D. R. Lowy, Laboratory of Cellular Oncology, National Cancer Institute, Bethesda, MD 20892.
P. G. Polakis and F. McCormick, Cetus Corporation, Emeryville, CA 94608.

*Present address: Pasteur Institute, Lille, France.

At least some members of the Ras superfamily can be regulated by more than one protein with GAP-like activity. Two distinct Rap-GAP molecules have been described (*6*, *8*) and designated cytoplasmic and membrane Rap-GAP, respectively, although some membrane Rap-GAP is in the cytosol (*9*). Interaction of Ras with Ras-GAP or with the GAP-related domain of the type 1 neurofibromatosis protein (NF1-GRD) increases its GTPase activity in vitro and inhibits its biological function in vivo in yeast (*10*, *11*). GTP-bound Ras is resistant to both forms of Rap-GAP, and GTP-bound Rap is resistant to NF1-GRD and to Ras-GAP although it interacts physically with Ras-GAP (*3*, *12*).

Experimentally induced overexpression of Ras-GAP can inhibit Ras activity in mammalian cells (*13*) and decrease the proportion of GTP-bound Ras (*14*). However, it is not known whether Ras is regulated under physiological conditions by Ras-GAP, NF1,